



Blocking oxygen evolution reaction for efficient organic electrooxidation coupling hydrogen production by using layered double hydroxide rich in active oxygen

Yingjie Song^a, Xin Wan^a, Yucong Miao^a, Jinze Li^a, Zhen Ren^a, Bowen Jin^a, Hua Zhou^{a,b}, Zhenhua Li^{a,b}, Mingfei Shao^{a,b,*}

^a State Key Laboratory of Chemical Resource Engineering, Beijing University of Chemical Technology, Beijing 100029, PR China

^b Quzhou Institute for Innovation in Resource Chemical Engineering, Quzhou 324000, PR China

ARTICLE INFO

Keywords:

Active oxygen
Layered double hydroxides
Amorphous
Glycerol oxidation
Hydrogen production

ABSTRACT

Electrochemical hydrogen production coupling upgrading of organic substances has been regarded as a promising approach to harvest both green energy and commodity products. However, the competition of oxygen evolution reaction always limits the transformation of organics and the research on this mutually restricted relationship was less focused. Herein, an amorphous layered double hydroxide (LDH) rich in active oxygen is well-constructed, which realizes the glycerol oxidation with nearly 100 % faradaic efficiency and high formic acid production yield at a current density $> 200 \text{ mA cm}^{-2}$. *In-situ* monitoring combined with electrochemical probe confirms that the active oxygen on the amorphous LDHs promotes the deprotonation of glycerol. To further reduce the energy input, an alkaline-acid hybrid flow cell is built to achieve constant hydrogen production coupling formic acid production at high current density (100 mA cm^{-1}) under an ultra-low cell voltage of 0.90 V with high durability for over 500 h. Moreover, a novel waste oil recycle path is developed to transform waste oil into target value-added products (potassium diformate (KDF) and biodiesel) and hydrogen fuels using the amorphous LDHs electrocatalysts.

1. Introduction

The exploration of hydrogen energy enables the reduction of fossil fuels consumption and greenhouse gas emission. Hereinto, hydrogen production via electrochemical water splitting has been regarded as the most promising and green approach by using electricity from renewable resources [1,2]. However, the oxygen evolution reaction (OER), as one of the half reaction of water splitting, presents formidable challenges to its widespread development and application due to the thermodynamically unfavorable four-electron redox process [3–6]. Besides, the oxygen product is not only low value-added but also explosive while mixing with hydrogen generated at cathode. To address above mentioned challenges, we have put forward electrochemical hydrogen-evolution coupled with alternative oxidation (EHCO) as an attractive strategy to achieve efficient production of both hydrogen and value-added chemicals/fuels by replacing water oxidation with oxidation of much easier oxidized molecules [7]. Using organic oxidation as an example, the

overpotential can be obviously reduced compared to OER along with the electrochemical selective transformation of the giving substances [8–10]. In particular, the upgrading of accessible glycerol is a rational alternative to OER, contributing to higher hydrogen production and synthesis of multiple value-added compounds [11–14]. Moreover, formic acid, as one of the products, is the fuel for direct formic acid fuel cells with high energy density and also a crucial platform molecule in chemical industry. However, the Faradic efficiency (FE) of organic oxidation by most electrocatalysts is not satisfactory due to the competition of OER, which makes contradiction of simultaneously improving the yield and selectivity of value-added products.

Both the water oxidation and organics oxidation involve the active oxygen species (AOS) transformation, which probably determines the directions of electrochemical oxidation when operated in a mixture media. Recent progresses on the studies of OER paid great attentions on the transformation of AOS at pristine aqueous media [15–19], while the activity origin and intermediates in organic oxidation based on AOS is

* Corresponding author at: State Key Laboratory of Chemical Resource Engineering, Beijing University of Chemical Technology, Beijing 100029, PR China.

E-mail address: shaomf@mail.buct.edu.cn (M. Shao).

¹ 0000-0002-6461-623X

<https://doi.org/10.1016/j.apcatb.2023.122808>

Received 17 January 2023; Received in revised form 10 March 2023; Accepted 25 March 2023

Available online 24 April 2023

0926-3373/© 2023 Elsevier B.V. All rights reserved.

rarely noted and investigated. Thus, the studies of AOS during organic oxidation will provide valuable clues about the competition between organic molecules and water for researchers to understand the rate determining step and mechanism. Moreover, the exploration of AOS may blaze a trail in the design of efficient electrocatalyst towards EHCO with higher selectivity under high energy utilizing efficiency.

Layered double hydroxides (LDHs) have received great interests as advanced electrocatalysts for OER due to the advantages of high activity and cost-effective [20,21]. Moreover, LDHs have been reported as efficient electrocatalysts for various organics upgrading, such as 5-hydroxymethylfurfural, glycerol and glucose [22–24]. However, similar to most electrocatalysts, it is hard to depress water oxidation in organic/water electrolyte by using LDHs due to their intrinsic high activity towards OER. Herein, we find that hydroxy group on the host layer of amorphous LDHs is more easily deprotonated at an ultralow voltage to generate active oxygen (Scheme 1), which can oxidize the alcohol molecules while suppressing OER. The amorphous NiFe-LDH can boost efficient glycerol oxidation with nearly 100 % FE (99.03 % at 1.47 V vs. RHE) and high formic acid production yield ($4.34 \text{ mol m}^{-2} \text{ h}^{-1}$) at a high current density over 200 mA^{-2} . Combining *in-situ* observation and chemical probes, the existence of multiple AOS and AOS involved oxidation mechanism is uncovered. Inspired by this finding, a hybrid EHCO cell consisting of alkaline anode chamber and acid cathode chamber is designed that boost electrochemical glycerol oxidation coupling hydrogen production with a high current density of 100 mA cm^{-2} under an ultra-low cell voltage of 0.90 V. To demonstrate the practical application, we conceived a new cycling path of waste oil into target value-added products (potassium diformate (KDF) and biodiesel) through the electrooxidation of crude glycerol coupled with hydrogen production.

2. Experimental section

2.1. Preparation of A-NiFe-LDH

Self-supported amorphous NiFe-LDH (A-NiFe-LDH) nanosheets arrays on Ni foam (Fig. S5) is fabricated via an electrochemical amorphization of crystallized NiFe-LDH that was prepared via the hydrothermal method (details see in supporting information). Typically, the NiFe-LDH was used as the anode and assembled into coin cells with Li disk as the cathode in an argon-filled glove box. The galvanostatic discharge process was performed at current of 0.5 mA with 12 h for the Li intercalation. After the discharge process, the Li metal-intercalated NiFe-LDH was extracted from the cell and transferred into alcohols to remove the

electrolyte and Li metal. Then the as-obtained A-NiFe-LDH was cleaned and dried at 60°C for further application.

2.2. Glycerol oxidation products measurements

The glycerol (GLY) oxidation measurements were performed by using a CHI760E electrochemical workstation and the products were analyzed using the high-performance liquid chromatography (HPLC, Shimadzu Prominence LC-20AT) with an ultraviolet-visible detector set at 210 nm and differential refraction detector. In each measurement, 200 μL of the electrolyte solution was withdrawn from the cell during chronoamperometry testing and diluted to 1.0 mL with dilute sulfuric acid solution and then 40 μL of the diluted solution was injected directly into a HPX-87 H column. Sulfuric acid (H_2SO_4 , 0.01 M) was used as the mobile phase with a constant flow rate of 0.6 mL/min and column temperature of 50°C . The identification of the GLY and its various oxidation products was achieved by comparing their retention times in the chromatograms with those of the standard solution, and their concentrations were determined from calibration curves by applying standard solutions with known concentrations. The Faradaic efficiencies toward GLY conversion to formic acid (FA) can be calculated by:

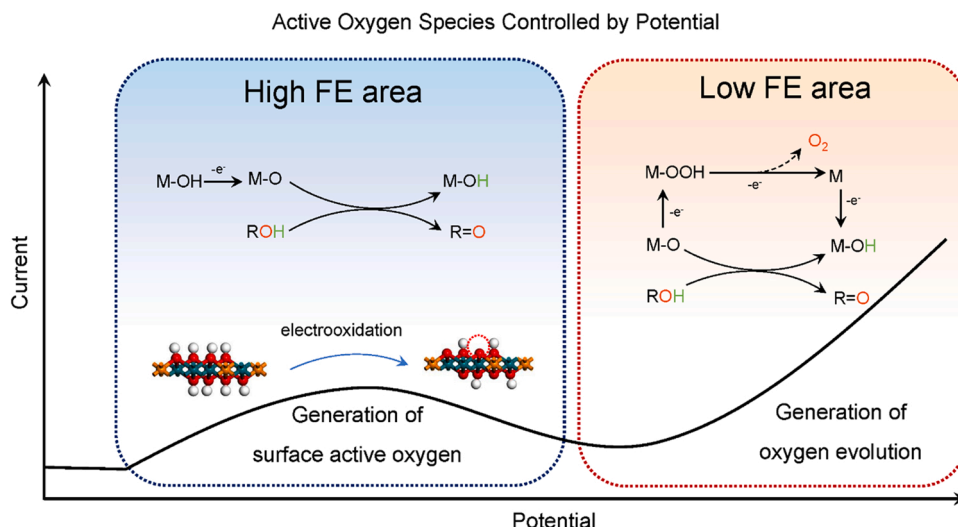
$$\text{FE} = \frac{8 \times N(\text{FA}) \times F}{3 \times Q}$$

Where 8/3 is 8 electrons are required to convert one GLY molecule to 3 FA molecule, $N(\text{FA})$ is the total amount (in units of moles) of FA obtained from chronoamperometry test, F is the Faraday constant ($F = 96485 \text{ C mol}^{-1}$), Q is the total charge passed through the electrochemical cell.

3. Results and discussion

3.1. Electrooxidation of glycerol over amorphous NiFe-LDH

The electrochemical property of NiFe-LDH with different crystallinity is first investigated by cyclic voltammetry (CV) in 1 M KOH electrolyte. As shown in Fig. 1a, an evident redox peak is observed for A-NiFe-LDH in the potential window of 1.40–1.50 V vs. RHE, while no obvious peak is recorded for the prepared NiFe-LDH. This suggest the much higher electrochemical activity of LDHs after amorphization treatment. After adding 0.1 M glycerol (GLY) into the electrolyte, the oxidation peak is disappeared and the onset potential shifts from 1.52 V to 1.35 V vs. RHE (Fig. 1b), implying the involvement of GLY oxidation reaction (GLYOR). Moreover, the lower onset potential of A-NiFe-LDH



Scheme 1. Schematic illustration of the AOS mechanism controlled by potential.

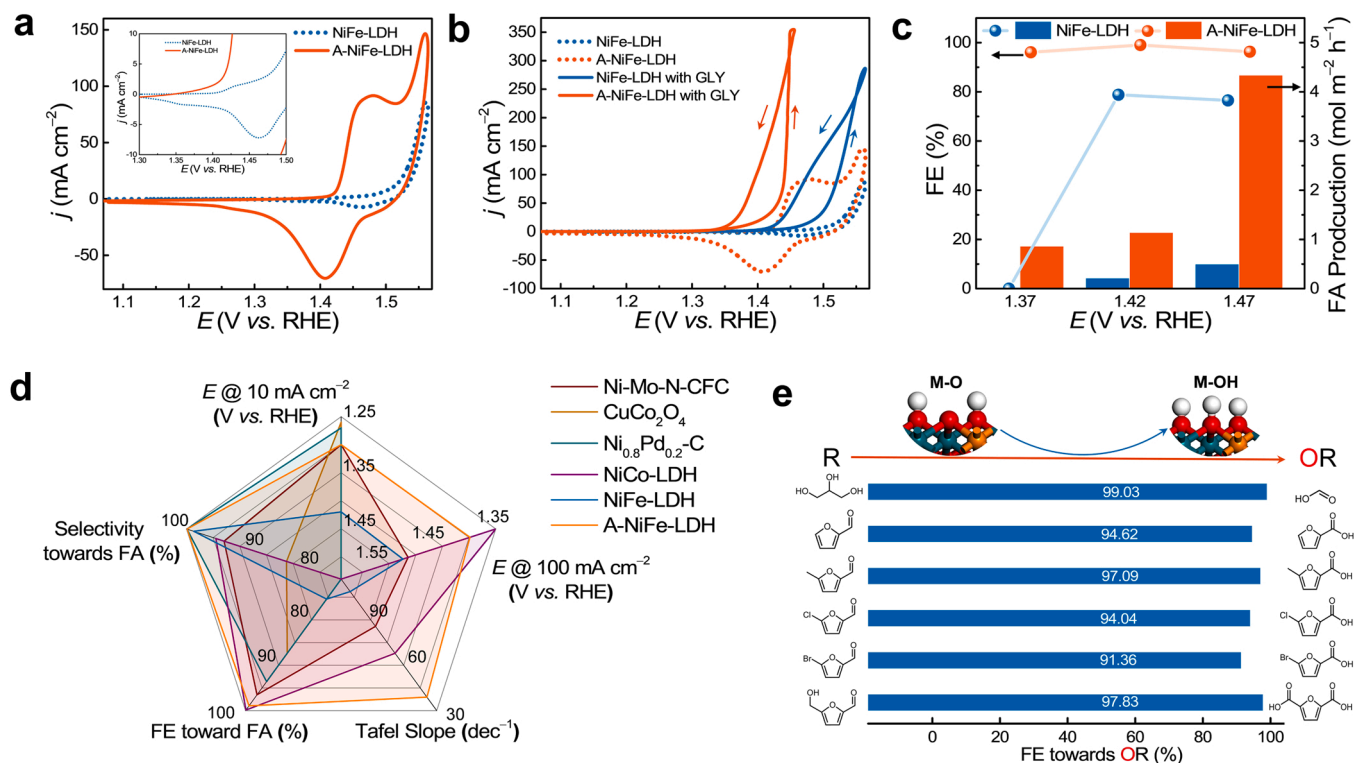


Fig. 1. (a) CV curves (90 % iR -corrected) of A-NiFe-LDH and NiFe-LDH at a scan rate of 5 mV s^{-1} in 1.0 M KOH . (b) CV curves (90 % iR -corrected) of A-NiFe-LDH and NiFe-LDH at a scan rate of 5 mV s^{-1} in 1.0 M KOH with and without 0.1 M glycerol. (c) FEs and FA production of A-NiFe-LDH and NiFe-LDH under different potentials. (d) Comparison of the electrooxidation performances of A-NiFe-LDH and reported catalysts. (e) FEs towards various products over A-NiFe-LDH.

compared to NiFe-LDH (1.42 V vs. RHE) further proves the much easier GLYOR in A-NiFe-LDH. The GLYOR performance of bare Ni foam is also evaluated and displayed in Fig. S2. Compared to A-NiFe-LDH and NiFe-LDH, the Ni foam exhibited greatly limited GLYOR activity with a low current density of 5.73 mA cm^{-2} at 1.42 V , much lower than that of A-NiFe-LDH ($\sim 200 \text{ mA cm}^{-2}$). To illustrate the outstanding performance of A-NiFe-LDH towards GLYOR, the products concentration in the electrolyte are evaluated by using high performance liquid chromatography (HPLC). As displayed in Fig. 1c, A-NiFe-LDH exhibits excellent performance towards GLYOR at an ultra-low potential of 1.37 V vs. RHE , while the crystallized NiFe-LDH shows no activity. Moreover, A-NiFe-LDH exhibits a rapid FA production rate of $4.34 \text{ mol m}^{-2} \text{ h}^{-1}$ under 1.47 V vs. RHE , which is 8 times higher than that of NiFe-LDH ($0.50 \text{ mol m}^{-2} \text{ h}^{-1}$). To exclude the interference of alkaline electrolyte towards glycerol, blank experiment with no current is performed. As shown in Fig. S3, barely no glycerol is converted into formic acid after standing in 1 M KOH for over 24 h. The kinetics of GLYOR over A-NiFe-LDH is also investigated. As shown in Fig. S4a, A-NiFe-LDH exhibits a Tafel slope of $39.12 \text{ mV dec}^{-1}$ for GLYOR, much lower than that of NiFe-LDH ($110.56 \text{ mV dec}^{-1}$), indicating a better GLYOR kinetic profile for A-NiFe-LDH. Additionally, the FEs towards FA of A-NiFe-LDH can maintain at a high level ($>95\%$) in the low potential window of $1.37\text{--}1.47 \text{ V vs. RHE}$ with no decrease in FE after eight GLYOR cycles under 1.47 V (Fig. S4b), demonstrating the excellent activity and stability. In contrast, the FEs towards GLYOR of crystallized NiFe-LDH is greatly limited ($<80\%$) under each applied potential due to the fierce competition of OER (Fig. 1c and Fig. S4d). It is worth mentioning that A-NiFe-LDH can reach a high current density of 100 mA cm^{-2} under much lower potential (1.40 V vs. RHE) with high FE and selectivity towards FA, much superior to former reported electrocatalysts (Fig. 1d and Table S5). Moreover, A-NiFe-LDH also exhibits high activity and selectivity in the oxidation of other alcohol and aldehyde. As shown in Fig. 1e, high FEs of 99.03 % and 97.83 % can be obtained for FA and 2,5-furandicarboxylic acid from the selectively upgrading of glycerol and 5-hydroxymethylfurfural,

indicating the great generality of amorphous LDHs in organic electrooxidation.

3.2. Structural and morphological characterizations of amorphous NiFe-LDH

To investigate the amorphous structure of A-NiFe-LDH, systematic morphological and structural characterization has been performed. Fig. 2a displays the top-view scanning electron microscopy (SEM) image of A-NiFe-LDH, where the unique spongy nanosheets array architecture is observed. The high-resolution transmission electron microscopy (HR-TEM) and corresponding SAED pattern of A-NiFe-LDH shows no lattice fringes and diffraction ring, confirming the amorphous nature (Fig. 2b). The Ni, Fe and O are uniformly distributed in A-NiFe-LDH after amorphization as revealed by energy dispersive X-ray (EDX) mapping results (Fig. 2c). Moreover, X-ray diffraction (XRD) pattern show no diffraction peaks for A-NiFe-LDH except for the peaks of Ni foam at 44.5° and 51.8° (Fig. S6), further indicating the successful amorphization process. In contrast, the well-crystallized NiFe-LDH without treatment gives clear (003), (006), (012) and (015) reflections of LDHs (Fig. 2d) [25,26].

X-ray absorption spectroscopy (XAS) is further employed to explore the local atomic arrangements in A-NiFe-LDH. The Ni K-edge X-ray absorption near edge structure (XANES) spectra of NiFe-LDH and A-NiFe-LDH show similar photon energy peak at $\sim 8350 \text{ eV}$ (Fig. 2e). The lower white line intensity of A-NiFe-LDH indicates a higher electron density and lower valance of Ni species in A-NiFe-LDH, which is consistent with the Ni 2p X-ray photoelectron spectroscopy (XPS) results in Fig. S7a [27]. The Ni K-edge Fourier transformed (FT) $k^3\chi(k)$ functions-R space curves for both NiFe-LDH and A-NiFe-LDH show two main peaks at 1.6 \AA and 2.7 \AA , corresponding to the Ni-O and Ni-M ($M = \text{Ni, Fe}$) coordination (Fig. 2f). The fitting results (Fig. S8 and Table S2) of A-NiFe-LDH indicate that the coordination number of Ni-O in the first shell decreases from 5.1 (NiFe-LDH) to 3.5 (A-NiFe-LDH), implying the

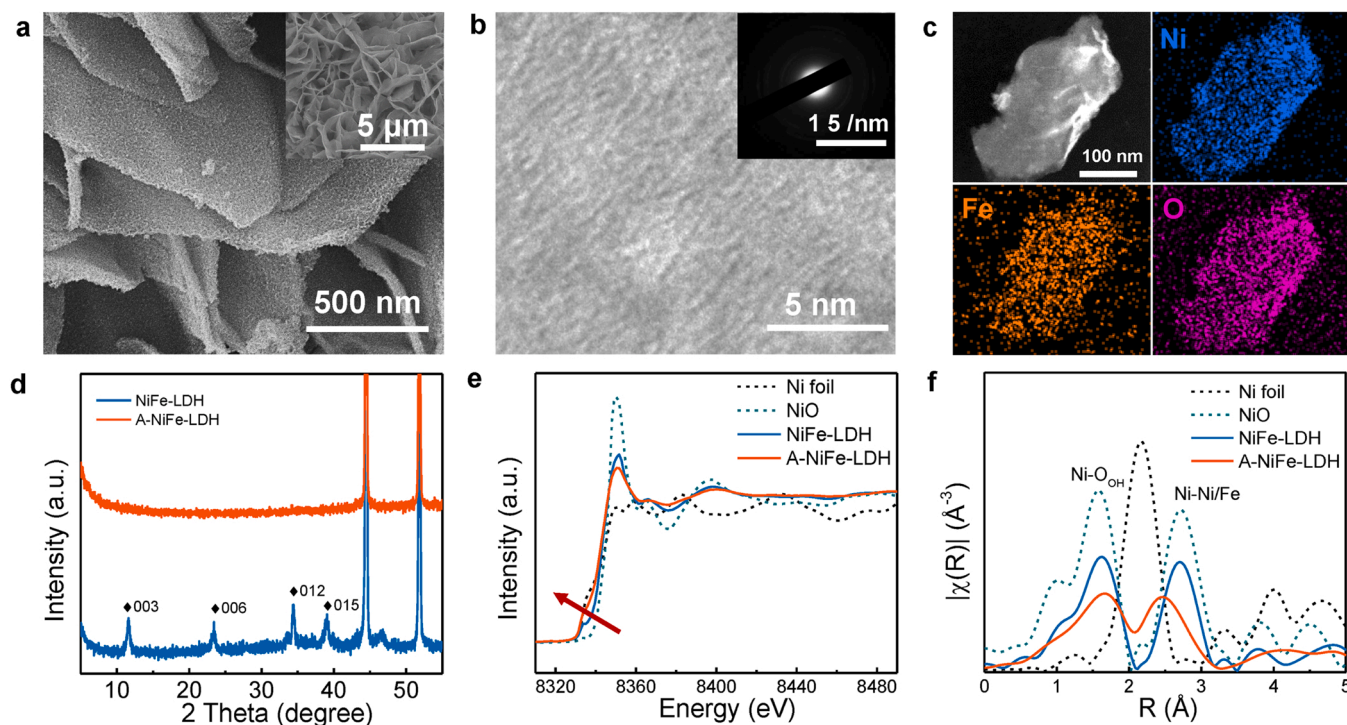


Fig. 2. (a) SEM images, (b) HR-TEM image and corresponding SEAD result and (c) TEM image and corresponding EDX mapping results of A-NiFe-LDH. (d) XRD patterns of A-NiFe-LDH and NiFe-LDH. (e) Ni K-edge XANES spectra for A-NiFe-LDH and NiFe-LDH. (f) Magnitude of k^2 -weighted Fourier transforms of the Ni K-edge XANES spectra for A-NiFe-LDH and NiFe-LDH.

fine structure change of Ni–O and the presence of oxygen vacancies in A-NiFe-LDH [28,29]. The O1s XPS (Fig. S7b) and electron paramagnetic resonance (EPR) spectrum (Fig. S7d) both confirm the presence of oxygen vacancies [30,31]. Besides, the coordination number of Ni–M in A-NiFe-LDH ($N = 4.9$) is significantly lower than that of NiFe-LDH ($N = 6.8$), indicating the formation of metal vacancies [32]. Likewise, the local atomic arrangement of Fe in A-NiFe-LDH is also investigated by XAS (Fig. S9), which suggests the presence of abundant oxygen and metal vacancies in A-NiFe-LDH [33]. The lower binding energy of A-NiFe-LDH in the Fe 2p XPS results (Fig. S7c) indicates a higher electron density and lower valance of Fe species in A-NiFe-LDH and no obvious Fe loss is observed after amorphization (Table S3). In comparison with NiFe-LDH, the greater Debye-Waller factor of A-NiFe-LDH (Table S2 and S4) reveals a more disordered structure around both Ni and Fe atoms [34]. The adsorption of glycerol on LDHs are also studied by open circuit potential (OCP) tests. As shown in Fig. S10, the OCP decreases by 59 mV for A-NiFe-LDH after adding 100 mM glycerol in the electrolyte, much greater than that of NiFe-LDH (35 mV), indicating a stronger adsorption of glycerol on the electrode. All above results indicate the amorphization process introduced enriched defect structure and unsaturated sites, which provides efficient active sites for electrocatalysis.

3.3. In-situ monitoring of AOS generation and AOS involved GLYOR mechanism

To precisely identify the process of GLYOR over A-NiFe-LDH, the dynamic changes of the electrocatalysts are monitored by *in-situ* Raman spectrum (Fig. 3a and Fig. S11). For NiFe-LDH, two peaks at 455 cm^{-1} and 534 cm^{-1} can be observed in 1 M KOH electrolyte, which are associated with $\text{Ni}^{\text{II}}\text{--OH}$ vibration in NiO_6 octahedron of NiFe-LDH [35]. When the applied potential is higher than 1.47 V vs. RHE, bands assigned to $\text{Ni}^{\text{III}}\text{--O}$ vibrations of NiOOH at 475 cm^{-1} and 553 cm^{-1} occurred, corresponding to the dehydrogenation of LDHs and the generation of surface AOS (Ni–O) [36,37]. In comparison, no peaks are

observed for A-NiFe-LDH in 1.0 M KOH, which could be ascribed to its amorphous properties. Moreover, the presence signal of $\text{Ni}^{\text{II}}\text{--OH}$ to $\text{Ni}^{\text{III}}\text{--O}$ just starts at 1.37 V vs. RHE in A-NiFe-LDH, with 100 mV lower than that of NiFe-LDH (1.47 V), which indicates the lower energy barrier for the dehydrogenation to generate surface AOS (Ni–O) in A-NiFe-LDH. In 1 M KOH electrolyte with 10 mM GLY, the peaks for $\text{Ni}^{\text{III}}\text{--O}$ vibrations of NiOOH do not appear until the potential rise up to 1.57 V vs. RHE, owing to the fast and spontaneous reaction between surface AOS (Ni–O) and GLY [38,39]. Accordingly, we can clearly identify that the surface AOS (Ni–O) plays a vital role in the activation and oxidation of GLY via the spontaneous reaction. Moreover, multi-potential step experiments are designed to build the connection between surface AOS (Ni–O) and GLYOR (Fig. S12). First, an anodic potential (1.57 V vs. RHE) is applied in 1 M KOH electrolyte and a positive current is occurred at this stage, corresponding to the formation of surface AOS (Ni–O). After a period of circuit breaking, a reduction potential is performed and an obvious negative current is generated, which can be assigned to the electrochemical consumption of surface AOS (Ni–O). Interestingly, the reduction current is disappeared after adding 100 mM GLY into the electrolyte during the circuit breaking stage, which indicates that the surface AOS (Ni–O) is consumed by GLY and the dehydrogenation of GLY by surface AOS (Ni–O) is a spontaneous process.

The GLYOR over A-NiFe-LDH is further monitored through *in-situ* attenuated total reflectance-infrared spectroscopy (ATR-IR, Fig. 3b and Fig. S13). As the applied potential increases to 1.37 V vs. RHE, three absorption bands located at 1353, 1385, 1580 cm^{-1} bands are generated, which can be assigned to the stretching vibration of O–C–O ($\nu_{\text{O–C–O}}$), bending vibration of C–H ($\delta_{\text{C–H}}$) and stretching vibration of C=O ($\nu_{\text{C=O}}$) of formate, respectively [40,41]. The intensity of these bands gradually increased as the applied potential increased (1.37–1.67 V vs. RHE), indicating relatively higher rates of formate generation and GLY consumption at higher potentials. Besides, the bands for carbonate at $\sim 1400 \text{ cm}^{-1}$ is not observed, suggesting the absence of over oxidation of formate into carbonate on the surface of

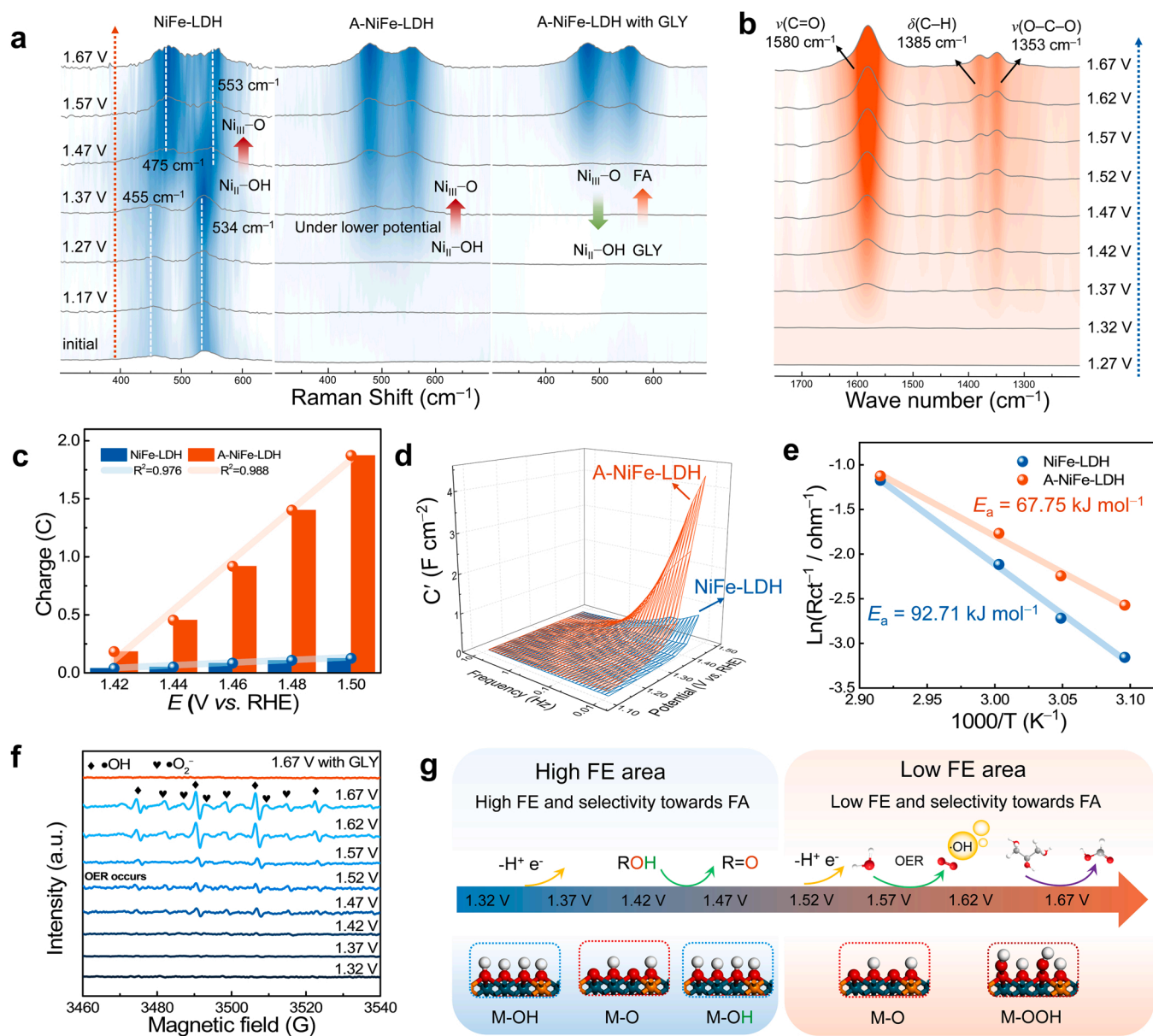


Fig. 3. (a) Potential-dependent *in-situ* Raman spectra of A-NiFe-LDH and NiFe-LDH. (b) Potential-dependent *in-situ* ATR-IR spectra of A-NiFe-LDH. (c) Charge of surface AOS (Ni-O) formation vs. potential for A-NiFe-LDH and NiFe-LDH in 1 M KOH. (d) 3D Bode plot of real area-normalized capacitance (C') of surface AOS (Ni-O) formation vs. frequency vs. potential for A-NiFe-LDH and NiFe-LDH in 1 M KOH. (e) Plots of $\ln(R_{ct}^{-1})$ vs. $1000/T$ of A-NiFe-LDH and NiFe-LDH. (f) Potential-dependent EPR spectra of radical adduct with DMPO of A-NiFe-LDH. (g) Schematic illustration of the AOS participated glycerol oxidation mechanism over A-NiFe-LDH.

A-NiFe-LDH. Moreover, the concentrations of GLY and possible products during the oxidation process were monitored by HPLC. As shown in Fig. S4c, the concentration of GLY is gradually decreased along with the accumulation of FA during the electrolysis process. In addition, small amount of glyceric acid, glycollic acid, lactic acid and oxalic acid are also detected as the intermediates. Based on above results, a possible pathway of glycerol oxidation over A-NiFe-LDH is concluded in Fig. S14. Firstly, glycerol is oxidized into glycerate with glyceraldehyde as possible intermediate in the oxidation path. In the second step, glycolate and formate are generated through the first C-C bond cleavage. Afterwards, glycolate is broke into two formate molecule through the second C-C bond cleavage. 8 electrons are consumed and 3 formate are generated in this glycerol oxidation reaction over A-NiFe-LDH.

The pulse voltammetry test is performed to evaluate the amount of surface AOS (Ni-O) generated under different applied potentials (Fig. S15). By integrating the cathodic current pulses, the amount of

oxidative charge that was stored in LDHs for the generation of surface AOS (Ni-O) can be obtained [42]. As shown in Fig. 3c, the charge of surface AOS generation for both NiFe-LDH and A-NiFe-LDH are increased along with the arise of applied potential for 1.42 – 1.50 V vs. RHE. Compared with NiFe-LDH, over 10 times more charge was stored in A-NiFe-LDH, indicating far greater amount of surface AOS (Ni-O) is formed under the applied anodic potential. Besides, the *in-situ* electrochemical impedance spectroscopy (EIS) results under different applied potential give out the same information. As shown in Fig. S16a, the resistances of A-NiFe-LDH start to decrease and semicircles occur when the applied potential rise to 1.32 V vs. RHE, which is consistent with the CV curves (Fig. 1b) and *in-situ* Raman spectrum (Fig. 3a). However, the Nyquist plots of NiFe-LDH under 1.12–1.47 V vs. RHE exhibit nearly vertical lines in 1 M KOH, indicating a huge charge transfer resistance owing to much slower formation progress of surface AOS (Ni-O) (Fig. S16b) [43]. Moreover, the above results can be also plotted in the

form of Bode plots with capacitance of expressed as the function of frequency, which provides a measure of how much charge was stored in the electrodes during the surface AOS (Ni–O) generation progress [44, 45]. As shown in Fig. 3d, the accumulated charge in A-NiFe-LDH is gradually increased along with the rise of potential while barely no charge is stored in NiFe-LDH within the same potential window, indicating a great more surface AOS (Ni–O) is formed in A-NiFe-LDH. The dynamic process of surface AOS (Ni–O) generation is further analyzed by CVs with different scan rate (Fig. S17). The peak current (i) of surface AOS (Ni–O) generation can be regarded as a function of scan rate (v) following the power law of $i = av^b$. By plotting $\log(i)$ vs. $\log(v)$, the b value can be obtained, which provides clues about the transport dynamics. For instance, a b value close to 0.5 represent sluggish process limited by slow electrons diffusion in catalysts [46]. As shown Fig. S18, the b value of A-NiFe-LDH is calculated to be 0.72, much higher than that of NiFe-LDH (0.5), indicating an accelerated process of surface AOS (Ni–O) generation in A-NiFe-LDH. Besides, the interfacial kinetics of surface AOS (Ni–O) generation in different electrodes can be further studied by temperature-dependent EIS (Fig. S19). The charge transfer resistance (R_{CT}) under different temperature can be evaluated through the fitting of EIS spectrum on the equivalent circuit shown in Fig. S20. The activation energy (E_a) of surface AOS (Ni–O) generation can be obtained by plotting $\ln(R_{CT}^{-1})$ vs. $1000/T$ [47,48]. As shown in Fig. 3e, A-NiFe-LDH required a much lower E_a of 67.75 kJ mol⁻¹ compared to NiFe-LDH (92.71 kJ mol⁻¹), illustrating a lower energy barrier of AOS (Ni–O) generation for A-NiFe-LDH. Therefore, the unique disordered structure of A-NiFe-LDH provides abundant active sites and reduce the energy barrier for the surface AOS generation to boost efficient GLYOR. The higher current density, lower activation energy and lower charge-transfer resistance of A-NiFe-LDH in GLYOR can be attributed its much higher surface area. Therefore, the change of electrochemical specific surface area (ECSA) for NiFe-LDH during the amorphization process should also be taken into consideration. The ECSA of A-NiFe-LDH and NiFe-LDH were calculated via the CV curves in non-Faradaic area to investigate the amount of active sites for surface AOS (Ni–O) generation. As shown in Fig. S21, the A-NiFe-LDH exhibits a 5-folds enhanced ECSA compared to NiFe-LDH.

The free radicals, as one kind of active oxygen specie, are also reported to be generated and effective in various oxidation reaction. Therefore, the oxygen radicals generated in the electrolyte for A-NiFe-LDH are also captured and detected via electron paramagnetic resonance (EPR) spectrum using as 5,5-dimethyl-1-pyrroline-N-oxide (DMPO) as the spin trap. As shown in Fig. 3f, no signal is found when the potential is lower than 1.47 V vs. RHE. Along with OER generation (applied potential > 1.47 V vs. RHE), four typical peaks for OH–DMPO adduct and three peaks for O₂–DMPO are occurred and the intensity of these peaks is gradually increased with rising potential, indicating the generation of hydroxyl radicals (·OH) and superoxide radical (·O₂) [49]. However, the peaks for ·OH and ·O₂ disappeared after adding 100 mM GLY into the electrolyte, attributed to the involvement of ·OH and ·O₂ in GLYOR. Meanwhile, the stronger signal of ·OH compared to ·O₂ implies a greater number of ·OH and its lead role in the GLYOR.

On the basis of above results, a clear AOS involved GLYOR mechanism over A-NiFe-LDH can be concluded in Fig. 3g. Firstly, A-NiFe-LDH is oxidized under lower potential (1.37 vs. RHE) along with the dehydrogenation. As the removal of hydrogen atom, the surface AOS (Ni–O) is generated and exposed, which can spontaneously seizure the hydrogen of GLY and active the following oxidation steps. Owing to the high selectivity and mild oxidation property of surface AOS (Ni–O), the GLY can be oxidized into FA with high FE and selectivity. However, the FE and selectivity towards GLYOR is slightly limited under higher applied potentials (>1.52 vs. RHE). This can be ascribed to the limited mass transfer of GLY, resulting adsorption of hydroxyl on surface AOS (Ni–O) and upcoming competition of OER at anode. Notedly, most of the surface AOS (Ni–O) can still act as the active sites for GLYOR and the generated hydroxyl radicals (·OH) also participate the GLYOR. In order

to maintain the high FE and high rate of GLYOR, broaden the surface AOS functional window and enhance the amount of surface AOS simultaneously is the rational strategy. Obviously, A-NiFe-LDH provides more surface AOS under much lower potential compared to pristine NiFe-LDH, verified by the 8 times-enhanced FA production under high FE.

3.4. Electrochemical GLYOR coupled with hydrogen production and waste-oil recycle over amorphous NiFe-LDH

To successfully achieve GLYOR coupling efficient hydrogen production, the hydrogen evolution reaction (HER) performance of the A-NiFe-LDH was further evaluated. A-NiFe-LDH exhibits an enhanced HER performance compared to NiFe-LDH with the overpotential of 228 mV to achieve 100 mA cm⁻² in 1 M KOH and the cathode products is confirmed to be hydrogen via gas chromatography (Fig. S22). Practically, huge energy input is inevitably required for electrochemical water splitting due to the high potential gap between OER and HER. Interestingly, the overpotential of two half-reaction can be flexibly adjusted by changing the pH of electrolyte based on the Nernst equation (Fig. 4a). With this mind, the cell voltage for water splitting can be theoretically decreased to 0.401 V when coupling an alkaline chamber with (pH = 14) an acid chamber (pH = 0) [11,50]. To achieve GLYOR coupling efficient hydrogen production under an ultra-low cell voltage, an alkaline-acid hybrid EHCO cell (Fig. S23) is assembled to further reduce the energy input of hydrogen production coupling GLYOR (Fig. 4b). Specifically, A-NiFe-LDH is used as anode with 1 M KOH and 100 mM GLY as anolyte while 20 % Pt/C on carbon fiber cloth is used as cathode with 0.5 M H₂SO₄ as catholyte. For comparison, the alkaline EHCO cell (1 M KOH with 100 mM GLY as anolyte and 1 M KOH as anolyte) and conventional overall water splitting cell (1 M KOH as anolyte and 1 M KOH as anolyte) is also built. As shown in Fig. 4c, the hybrid EHCO cell can drive a high current density of 500 mA cm⁻² with the cell voltage of only 1.72 V. Notably, extremely low cell voltage of 0.32 V, 0.76 V and 0.90 V are needed to reach the current density of 10 mA cm⁻², 50 mA cm⁻² and 100 mA cm⁻² respectively (Fig. 4d). In contrast, huge voltages of 1.52 V, 1.76 V and 1.98 V are required to achieve the same current density for the conventional overall water splitting cell. Moreover, the long-term durability of the hybrid EHCO cell is also taken into consideration. The pH in the anode chamber will decrease while the pH in the cathode chamber will increase gradually during electrolysis over time. This can be ascribed to the generation of formic acid in anode and consumption of proton in cathode. As shown in Fig. 4e, the cell voltage to reach the current density of 10 mA cm⁻² is increased from ~0.90 V to ~1.50 V after 100 h operation, which is still greatly lower than that of conventional alkaline water splitting cell (1.98 V). Moreover, after refreshing the electrolyte at both sides, the voltage at 100 mA cm⁻² returned to the same level of ~0.9 V. The total operation time lasted for over 500 h and barely no decline is observed, indicating the excellent stability of the hybrid EHCO cell. The XPS spectrum is conducted to investigate the valance change in A-NiFe-LDH after GLYOR. As shown in Fig. S24a, barely no change is observed for the electron density around Ni species in A-NiFe-LDH, indicating the rapid reaction between surface AOS and GLY. Meanwhile, the XRD spectrum, SEM and HR-TEM confirm that the amorphous feature and nanoarray structure is well maintained for A-NiFe-LDH after cycles (Fig. S24b–d).

To demonstrate the practical application, an EHCO waste oil recycle path is developed to transform waste oil into biodiesel and hydrogen fuels using A-NiFe-LDH electrocatalysts (Fig. 5a). In the conventional path, the pretreated waste oil usually undergoes the alkali-catalyzed transesterification reaction with methanol to form fatty ester (biodiesel) and the crude GLY is also obtained as the main by-product [51, 52]. However, high cost and time-consuming purification/separation are indispensable to remove the excess methanol and alkaline in crude GLY (such as KOH and NaOH) in order to meet up the standard for further use in chemical industry. In our EHCO recycle path, the

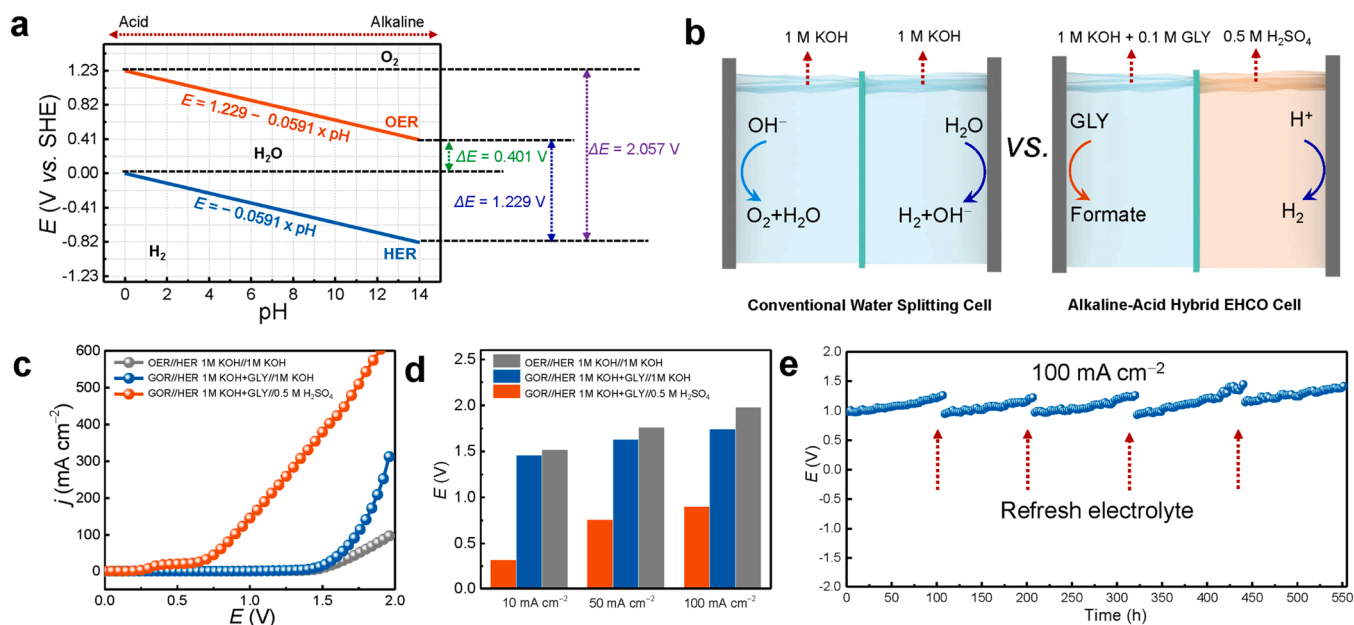


Fig. 4. (a) Pourbaix diagram with theoretical potentials for water splitting reactions. (b) Schematic illustration of hybrid alkali-acid electrolyzer based on A-NiFe-LDH. (c) LSV curves and (d) Voltage to reach different current densities of electrolyzer with different electrolyte composition. (e) Long-term stability test of hybrid alkali-acid electrolyzer based on A-NiFe-LDH under the current density of 100 mA cm⁻².

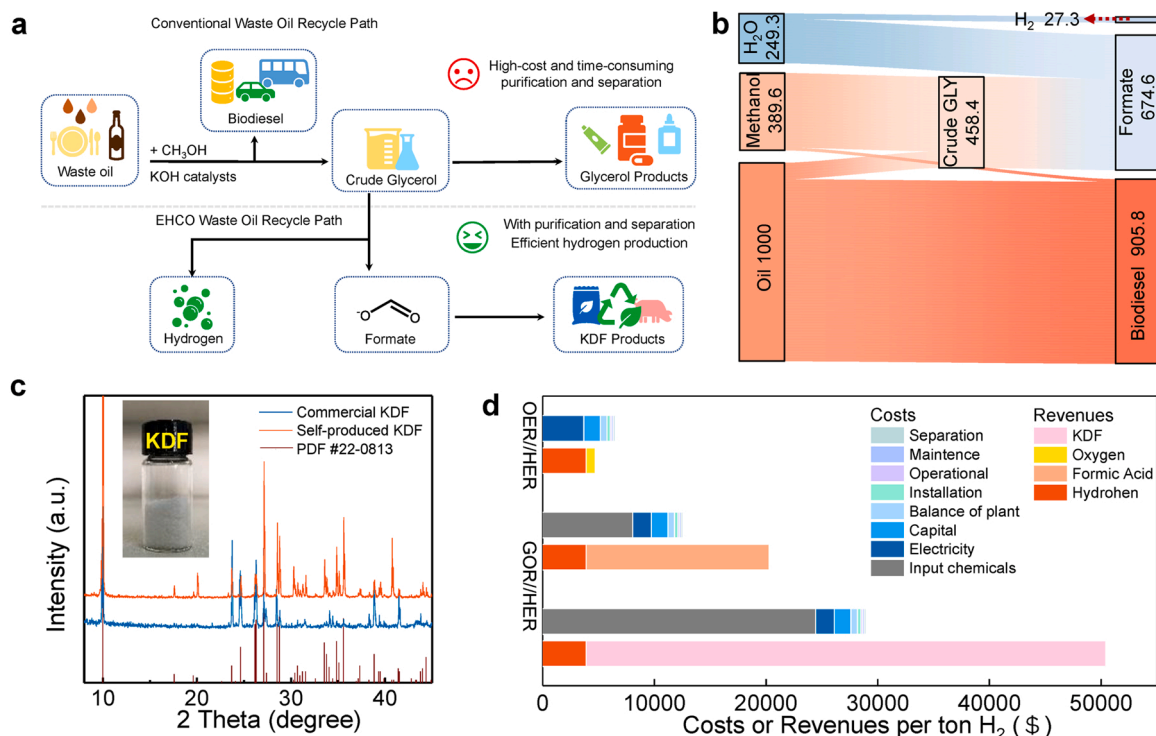


Fig. 5. (a) Schematic illustration and of waste oil recycle path. (b) Sankey diagram for the mass flow of EHCO waste oil recycle path. (c) XRD patterns of commercial KDF and self-produced KDF through waste oil recycle path. (d) Techno-economic analysis of hydrogen production via electrochemical water splitting.

as-obtained glycerol and excess methanol can be both oxidized into the same product (formate) and excess alkaline can serve as the electrolyte. Moreover, the resultant electrolyte from EHCO cell can be easily transformed into KDF by acidified to pH = 3 with formic acid, which avoids complex and expensive separation processes of oxidation product. The as-obtained KDF has been authorized as a safe alternative of antibiotic for promoting animal growth, which is useful in increasing the nutrient uptake and survive rate. The mass flow analysis of the EHCO recycle

path is conducted and shown in the Sankey diagram (Fig. 5b). As a result, 1 kg of pretreated waste oil can finally turn into 905.8 g biodiesel (Fig. S25a), 674.6 g formate and 27.3 g hydrogen gas. Subsequently, commodity chemicals KDF can be further obtained through neutralization and crystallization with the yield of 72.8 % for highly-pure KDF product (Fig. S25b). The purity of as-obtained KDF product is confirmed with XRD (Fig. 5c) and Fourier transformation infrared spectroscopy (FT-IR, Fig. S25c) and further examined and evaluated to be 99.63 %

based on the HPLC results (Fig. S25d). Moreover, the long-time oxidation stability test of crude GLY obtained from waste oil recycle is performed. As shown in Fig. S26, the cell voltage to reach 100 mA cm^{-1} in ECHO hybrid cell using crude GLY can maintain at $\sim 0.90 \text{ V}$ within 4 oxidation cycles. It is noteworthy that the EHCO recycle path can not only decrease the energy input of hydrogen production compared to conventional electrochemical water splitting, but also upgrade the total revenue through the value-added products. With this mind, the techno-economic analysis (TEA) is performed to estimate the net revenues of different hydrogen production strategy (Fig. 5d) [53,54]. The conventional electrochemical water splitting is still at a loss due to the high input of electricity and low value of oxygen product. By replacing OER with GLYOR, the energy input is successfully decreased and the value of products increased, leading to a positive net revenue of ~ 7817 \$ per ton hydrogen. Moreover, higher profitability with net revenue of ~ 21549 \$ per ton hydrogen can be achieved if all the formate is transformed into KDF products.

4. Conclusion

In summary, the A-NiFe-LDH nanosheet array electrocatalyst has been constructed for efficient glycerol oxidation coupling hydrogen production with high selectivity towards formic acid (FA, production = $4.34 \text{ mol m}^{-1} \text{ h}^{-1}$ with FE > 95 %). We confirm that A-NiFe-LDH can generated much more surface AOS with lower energy barrier, leading to extraordinary glycerol oxidation performance. Taking advantages of *in-situ* observation and electrochemical probe, the existence of multiple AOS and surface AOS involved oxidation mechanism is presented. Moreover, a hybrid EHCO electrolyzer is assembled based on A-NiFe-LDH nanosheet array electrode, which can achieve a high current density of 100 mA cm^{-2} under an ultra-low cell voltage of 0.90 V and 500 mA cm^{-2} at 1.72 V . Through a new cycling path, we successfully transformed waste oil into target value-added products (KDF and biodiesel) and hydrogen fuels.

CRediT authorship contribution statement

M. Shao led the project. Y. Song conducted material synthesis, carried out the catalytic performance test and wrote the paper. Y. Miao, J. Li, Z. Ren, B. Jin, H. Zhou and Z. Li assisted with the experiments. The manuscript was primarily written by Y. Song and M. Shao revised. All authors contributed to discussions and manuscript review.

Declaration of Competing Interest

The authors declare that they have no known competing financial interests or personal relationships that could have appeared to influence the work reported in this paper.

Data availability

Data will be made available on request.

Acknowledgments

This work was supported by the National Natural Science Foundation of China (22090031, 22090030, 22288102 and 21871021), Project funded by China Postdoctoral Science Foundation (2021M690319).

Appendix A. Supporting information

Supplementary data associated with this article can be found in the online version at doi:10.1016/j.apcatb.2023.122808.

References

- [1] S.Z. Oener, M.J. Foster, S.W. Boettcher, Accelerating water dissociation in bipolar membranes and for electrocatalysis, *Science* 369 (2020) 1099–1103.
- [2] Y. Liu, K. Zhang, K. Wang, M. Wang, Y. Liu, J. Jiang, T. Liu, E. Liang, B. Li, Out-of-plane CoRu nanoalloy axially coupling CoNC for electron enrichment to boost hydrogen production, *Appl. Catal. B Environ.* 318 (2022), 121890.
- [3] F.T. Haase, A. Bergmann, T.E. Jones, J. Timoshenko, A. Herzog, H.S. Jeon, C. Rettenmaier, B.R. Cuenya, Size effects and active state formation of cobalt oxide nanoparticles during the oxygen evolution reaction, *Nat. Energy* 7 (2022) 765–773.
- [4] L.C. Seitz, C.F. Dickens, K. Nishio, Y. Hikita, J. Montoya, A. Doyle, C. Kirk, A. Vojvodic, H.Y. Hwang, J.K. Nørskov, A highly active and stable $\text{IrO}_2/\text{SrIrO}_3$ catalyst for the oxygen evolution reaction, *Science* 353 (2016) 1011–1014.
- [5] C.-J. Huang, H.-M. Xu, T.-Y. Shuai, Q.-N. Zhan, Z.-J. Zhang, G.-R. Li, A review of modulation strategies for improving catalytic performance of transition metal phosphides for oxygen evolution reaction, *Appl. Catal. B Environ.* (2022), 122313.
- [6] Y. Gu, S. Wang, H. Shi, J. Yang, S. Li, H. Zheng, W. Jiang, J. Liu, X. Zhong, J. Wang, Atomic Pt embedded in BNC nanotubes for enhanced electrochemical ozone production via an oxygen intermediate-rich local environment, *ACS Catal.* 11 (2021) 5438–5451.
- [7] Y. Song, K. Ji, H. Duan, M. Shao, Hydrogen production coupled with water and organic oxidation based on layered double hydroxides, *Exploration* 1 (2021), 20210050.
- [8] Y. Song, Z. Li, K. Fan, Z. Ren, W. Xie, Y. Yang, M. Shao, M. Wei, Ultrathin layered double hydroxides nanosheets array towards efficient electrooxidation of 5-hydroxymethylfurfural coupled with hydrogen generation, *Appl. Catal. B Environ.* 299 (2021), 120669.
- [9] H. Sun, L. Li, Y. Chen, H. Kim, X. Xu, D. Guan, Z. Hu, L. Zhang, Z. Shao, W. Jung, Boosting ethanol oxidation by NiOOH-CuO nano-heterostructure for energy-saving hydrogen production and biomass upgrading, *Appl. Catal. B Environ.* (2023), 122388.
- [10] X. Luo, X. Tang, J. Ni, B. Wu, C. Li, M. Shao, Z. Wei, Electrochemical oxidation of styrene to benzaldehyde by discrimination of spin-paired π electrons, *Chem. Sci.* 14 (2023) 1679–1686.
- [11] L. Fan, Y. Ji, G. Wang, J. Chen, K. Chen, X. Liu, Z. Wen, High entropy alloy electrocatalytic electrode toward alkaline glycerol valorization coupling with acidic hydrogen production, *J. Am. Chem. Soc.* 144 (2022) 7224–7235.
- [12] X. Han, H. Sheng, C. Yu, T.W. Walker, G.W. Huber, J. Qiu, S. Jin, Electrocatalytic oxidation of glycerol to formic acid by CuCo_2O_4 spinel oxide nanostructure catalysts, *ACS Catal.* 10 (2020) 6741–6752.
- [13] Z. He, J. Hwang, Z. Gong, M. Zhou, N. Zhang, X. Kang, J.W. Han, Y. Chen, Promoting biomass electrooxidation via modulating proton and oxygen anion intercalation in hydroxide, *Nat. Commun.* 13 (2022) 3777.
- [14] Y. Song, W. Xie, Y. Song, H. Li, S. Li, S. Jiang, J.Y. Lee, M. Shao, Bifunctional integrated electrode for high-efficient hydrogen production coupled with 5-hydroxymethylfurfural oxidation, *Appl. Catal. B Environ.* 312 (2022), 121400.
- [15] Y. Hao, Y. Li, J. Wu, L. Meng, J. Wang, C. Jia, T. Liu, X. Yang, Z.-P. Liu, M. Gong, Recognition of surface oxygen intermediates on NiFe oxyhydroxide oxygen-evolving catalysts by homogeneous oxidation reactivity, *J. Am. Chem. Soc.* 143 (2021) 1493–1502.
- [16] H.B. Tao, Y. Xu, X. Huang, J. Chen, L. Pei, J. Zhang, J.G. Chen, B. Liu, A general method to probe oxygen evolution intermediates at operating conditions, *Joule* 3 (2019) 1498–1509.
- [17] S. Lee, L. Bai, X. Hu, Deciphering iron-dependent activity in oxygen evolution catalyzed by nickel-iron layered double hydroxide, *Angew. Chem. Int. Ed.* 59 (2020) 8072–8077.
- [18] F. Dionigi, Z. Zeng, I. Sinev, T. Merzdorf, S. Deshpande, M.B. Lopez, S. Kunze, I. Zegkinoglou, H. Sarodnik, D. Fan, In-situ structure and catalytic mechanism of NiFe and CoFe layered double hydroxides during oxygen evolution, *Nat. Commun.* 11 (2020) 1–10.
- [19] H. Zhou, Z. Li, S.M. Xu, L. Lu, M. Xu, K. Ji, R. Ge, Y. Yan, L. Ma, X. Kong, Selectively upgrading lignin derivatives to carboxylates through electrochemical oxidative C(OH)–C bond cleavage by a Mn-doped cobalt oxyhydroxide catalyst, *Angew. Chem. Int. Ed.* 60 (2021) 8976–8982.
- [20] M. Gong, Y. Li, H. Wang, Y. Liang, J.Z. Wu, J. Zhou, J. Wang, T. Regier, F. Wei, H. Dai, An advanced Ni–Fe layered double hydroxide electrocatalyst for water oxidation, *J. Am. Chem. Soc.* 135 (2013) 8452–8455.
- [21] M. Shao, R. Zhang, Z. Li, M. Wei, D.G. Evans, X. Duan, Layered double hydroxides toward electrochemical energy storage and conversion: design, synthesis and applications, *Chem. Commun.* 51 (2015) 15880–15893.
- [22] M. Shao, F. Ning, J. Zhao, M. Wei, D.G. Evans, X. Duan, Hierarchical layered double hydroxide microspheres with largely enhanced performance for ethanol electrooxidation, *Adv. Funct. Mater.* 23 (2013) 3513–3518.
- [23] W.-J. Liu, L. Dang, Z. Xu, H.-Q. Yu, S. Jin, G.W. Huber, Electrochemical oxidation of 5-hydroxymethylfurfural with NiFe layered double hydroxide (LDH) nanosheet catalysts, *ACS Catal.* 8 (2018) 5533–5541.
- [24] W.-J. Liu, Z. Xu, D. Zhao, X.-Q. Pan, H.-C. Li, X. Hu, Z.-Y. Fan, W.-K. Wang, G.-H. Zhao, S. Jin, Efficient electrochemical production of glucaric acid and H₂ via glucose electrolysis, *Nat. Commun.* 11 (2020) 1–11.
- [25] C. Zhang, M. Shao, L. Zhou, Z. Li, K. Xiao, M. Wei, Hierarchical NiFe layered double hydroxide hollow microspheres with highly-efficient behavior toward oxygen evolution reaction, *ACS Appl. Mater. Interfaces* 8 (2016) 33697–33703.
- [26] P. Li, X. Duan, Y. Kuang, Y. Li, G. Zhang, W. Liu, X. Sun, Tuning electronic structure of NiFe layered double hydroxides with vanadium doping toward high efficient electrocatalytic water oxidation, *Adv. Energy Mater.* 8 (2018), 1703341.

- [27] L. Zhou, M. Shao, C. Zhang, J. Zhao, S. He, D. Rao, M. Wei, D.G. Evans, X. Duan, Hierarchical CoNi-sulfide nanosheet arrays derived from layered double hydroxides toward efficient hydrazine electrooxidation, *Adv. Mater.* 29 (2017), 1604080.
- [28] B. Wang, X. Han, C. Guo, J. Jing, C. Yang, Y. Li, A. Han, D. Wang, J. Liu, Structure inheritance strategy from MOF to edge-enriched NiFe-LDH array for enhanced oxygen evolution reaction, *Appl. Catal. B Environ.* 298 (2021), 120580.
- [29] X. Zhang, Y. Zhao, Y. Zhao, R. Shi, G.I. Waterhouse, T. Zhang, A simple synthetic strategy toward defect-rich porous monolayer NiFe-layered double hydroxide nanosheets for efficient electrocatalytic water oxidation, *Adv. Energy Mater.* 9 (2019), 1900881.
- [30] M. Asnavandi, Y. Yin, Y. Li, C. Sun, C. Zhao, Promoting oxygen evolution reactions through introduction of oxygen vacancies to benchmark NiFe-OOH catalysts, *ACS Energy Lett.* 3 (2018) 1515–1520.
- [31] Y. Luo, Y. Wu, D. Wu, C. Huang, D. Xiao, H. Chen, S. Zheng, P.K. Chu, NiFe-Layered double hydroxide synchronously activated by heterojunctions and vacancies for the oxygen evolution reaction, *ACS Appl. Mater. Interfaces* 12 (2020) 42850–42858.
- [32] Z. Yuan, S.-M. Bak, P. Li, Y. Jia, L. Zheng, Y. Zhou, L. Bai, E. Hu, X.-Q. Yang, Z. Cai, Activating layered double hydroxide with multivacancies by memory effect for energy-efficient hydrogen production at neutral pH, *ACS Energy Lett.* 4 (2019) 1412–1418.
- [33] Y. Wang, Y. Zhang, Z. Liu, C. Xie, S. Feng, D. Liu, M. Shao, S. Wang, Layered double hydroxide nanosheets with multiple vacancies obtained by dry exfoliation as highly efficient oxygen evolution electrocatalysts, *Angew. Chem. Int. Ed.* 56 (2017) 5867–5871.
- [34] R. Liu, Y. Wang, D. Liu, Y. Zou, S. Wang, Water-plasma-enabled exfoliation of ultrathin layered double hydroxide nanosheets with multivacancies for water oxidation, *Adv. Mater.* 29 (2017), 1701546.
- [35] L. Peng, N. Yang, Y. Yang, Q. Wang, X. Xie, D. Sun-Waterhouse, L. Shang, T. Zhang, G.I. Waterhouse, Atomic cation-vacancy engineering of NiFe-layered double hydroxides for improved activity and stability towards the oxygen evolution reaction, *Angew. Chem.* 133 (2021) 24817–24824.
- [36] B.J. Trzeźniewski, O. Diaz-Morales, D.A. Vermaas, A. Longo, W. Bras, M.T. Koper, W.A. Smith, In situ observation of active oxygen species in Fe-containing Ni-based oxygen evolution catalysts: the effect of pH on electrochemical activity, *J. Am. Chem. Soc.* 137 (2015) 15112–15121.
- [37] S. Lee, K. Banjac, M. Lingenfelder, X. Hu, Oxygen isotope labeling experiments reveal different reaction sites for the oxygen evolution reaction on nickel and nickel iron oxides, *Angew. Chem. Int. Ed.* 58 (2019) 10295–10299.
- [38] W. Chen, C. Xie, Y. Wang, Y. Zou, C.-L. Dong, Y.-C. Huang, Z. Xiao, Z. Wei, S. Du, C. Chen, Activity origins and design principles of nickel-based catalysts for nucleophile electrooxidation, *Chem* 6 (2020) 2974–2993.
- [39] Y. Huang, X. Chong, C. Liu, Y. Liang, B. Zhang, Boosting hydrogen production by anodic oxidation of primary amines over a NiSe nanorod electrode, *Angew. Chem. Int. Ed.* 57 (2018) 13163–13166.
- [40] C.C. Lima, M.V.F. Rodrigues, A.F.M. Neto, C.R. Zanata, C.T.G.V.M.T. Pires, L. S. Costa, J. Solla-Gullón, P.S. Fernández, Highly active Ag/C nanoparticles containing ultra-low quantities of sub-surface Pt for the electrooxidation of glycerol in alkaline media, *Appl. Catal. B Environ.* 279 (2020).
- [41] F. Yang, J. Ye, Q. Yuan, X. Yang, Z. Xie, F. Zhao, Z. Zhou, L. Gu, X. Wang, Ultrasmall Pd-Cu-Pt trimetallic twin icosahedrons boost the electrocatalytic performance of glycerol oxidation at the operating temperature of fuel cells, *Adv. Funct. Mater.* 30 (2020).
- [42] H.N. Nong, L.J. Falling, A. Bergmann, M. Klingenhof, H.P. Tran, C. Spori, R. Mom, J. Timoshenko, G. Zichittella, A. Knop-Gericke, S. Piccinin, J. Perez-Ramirez, B. R. Cuenya, R. Schlogl, P. Strasser, D. Teschner, T.E. Jones, Key role of chemistry versus bias in electrocatalytic oxygen evolution, *Nature* 587 (2020) 408–413.
- [43] Z. Xiao, Y.-C. Huang, C.-L. Dong, C. Xie, Z. Liu, S. Du, W. Chen, D. Yan, L. Tao, Z. Shu, Operando identification of the dynamic behavior of oxygen vacancy-rich Co₃O₄ for oxygen evolution reaction, *J. Am. Chem. Soc.* 142 (2020) 12087–12095.
- [44] P. Taberna, P. Simon, J.-F. Fauvarque, Electrochemical characteristics and impedance spectroscopy studies of carbon-carbon supercapacitors, *J. Electrochem. Soc.* 150 (2003) A292.
- [45] J.S. Ko, M.B. Sassin, D.R. Rolison, J.W. Long, Deconvolving double-layer, pseudocapacitance, and battery-like charge-storage mechanisms in nanoscale LiMn₂O₄ at 3D carbon architectures, *Electrochim. Acta* 275 (2018) 225–235.
- [46] H. Lindström, S. Södergren, A. Solbrand, H. Rensmo, J. Hjelm, A. Hagfeldt, S.-E. Lindquist, Li⁺ ion insertion in TiO₂ (anatase). 2. Voltammetry on nanoporous films, *J. Phys. Chem. B* 101 (1997) 7717–7722.
- [47] D. Kundu, S.H. Vajargah, L. Wan, B. Adams, D. Prendergast, L.F. Nazar, Aqueous vs. nonaqueous Zn-ion batteries: consequences of the desolvation penalty at the interface, *Energy Environ. Sci.* 11 (2018) 881–892.
- [48] Y. Mizuno, M. Okubo, E. Hosono, T. Kudo, H. Zhou, K. Oh-ishi, Suppressed activation energy for interfacial charge transfer of a Prussian blue analog thin film electrode with hydrated ions (Li⁺, Na⁺, and Mg²⁺), *J. Phys. Chem. C* 117 (2013) 10877–10882.
- [49] H. Xie, X. Xie, G. Hu, V. Prabhakaran, S. Saha, L. Gonzalez-Lopez, A.H. Phakatkar, M. Hong, M. Wu, R. Shahbazian-Yassar, V. Ramani, M.I. Al-Sheikhly, D.-e. Jiang, Y. Shao, L. Hu, Ta–TiO_x nanoparticles as radical scavengers to improve the durability of Fe–N–C oxygen reduction catalysts, *Nat. Energy* 7 (2022) 281–289.
- [50] Y. Ding, P. Cai, Z. Wen, Electrochemical neutralization energy: from concept to devices, *Chem. Soc. Rev.* 50 (2021) 1495–1511.
- [51] D.Y.C. Leung, X. Wu, M.K.H. Leung, A review on biodiesel production using catalyzed transesterification, *Appl. Energy* 87 (2010) 1083–1095.
- [52] G. Dodekatos, S. Schünemann, H. Tüysüz, Recent advances in thermo-, photo-, and electrocatalytic glycerol oxidation, *ACS Catal.* 8 (2018) 6301–6333.
- [53] P. De Luna, C. Hahn, D. Higgins, S.A. Jaffer, T.F. Jaramillo, E.H. Sargent, What would it take for renewably powered electrosynthesis to displace petrochemical processes? *Science* 364 (2019) eaav3506.
- [54] Y. Lum, J.E. Huang, Z. Wang, M. Luo, D.-H. Nam, W.R. Leow, B. Chen, J. Wicks, Y. C. Li, Y. Wang, Tuning OH binding energy enables selective electrochemical oxidation of ethylene to ethylene glycol, *Nat. Catal.* 3 (2020) 14–22.